Supplementary Material

Stabilizing *CO intermediate on nitrogen-doped carbon-coated CuxOy derived from metal-organic framework for enhanced electrochemical CO_2-to-ethylene

Na Zhang,*[a] and Yunlong Zhang [b]

[a] State Key Laboratory of Fine Chemicals, School of Chemical Engineering, Dalian University of Technology, Dalian 116024, China.

[b] School of Chemistry and Chemical Engineering, Shanghai Jiao Tong University, Shanghai 200240, China.

Experimental Section

Materials and chemicals.

Potassium hydroxide (KOH, ≥85%), sodium hydroxide (NaOH, ≥96%), sodium bicarbonate ($NaHCO_3$, ≥99.5%), and potassium bicarbonate ($KHCO_3$, ≥99.5%) were purchased from Sinopharm Chemical Reagent (China). Copper(II) nitrate trihydrate ($Cu(NO_3)_2 \cdot 3H_2O$, ≥99.0%), 5-aminoisophthalic acid (98%), cyanogen chloride (99%), and CuO powder (99.5%) were provided by Macklin Biochemical Technology Co., Ltd. (China). These chemicals were used as received without further purification. Ultrapure water (18.2 MΩ cm at 25 ºC) was obtained from the Millipore water system (Synergy UV, France).

Synthesis of the organic ligand H_6TDPAT.

The ligand 2,4,6-tris(3,5-dicarboxylphenylamino)-1,3,5-triazine (H_6TDPAT) was synthesized with minor modifications based on the literature (Scheme 1).[1] 15.2 g 5-aminoisophthalic acid, 5.36 g NaOH, and 8.74 g $NaHCO_3$ were dissolved in 140 mL H_2O and stirred at 0 ºC for 30 min. The cyanogen chloride (3.68 g) was dissolved in 70 mL of 1,4-dioxane and added dropwise to the first solution. The solution was subsequently heated at reflux in an oil bath at 100 ºC for 17 h. Following natural cooling, the pH of the solution was adjusted to 2 by using HCl. The solid was then filtered, washed multiple times with distilled water, and dried to yield the ligand H_6TDPAT.

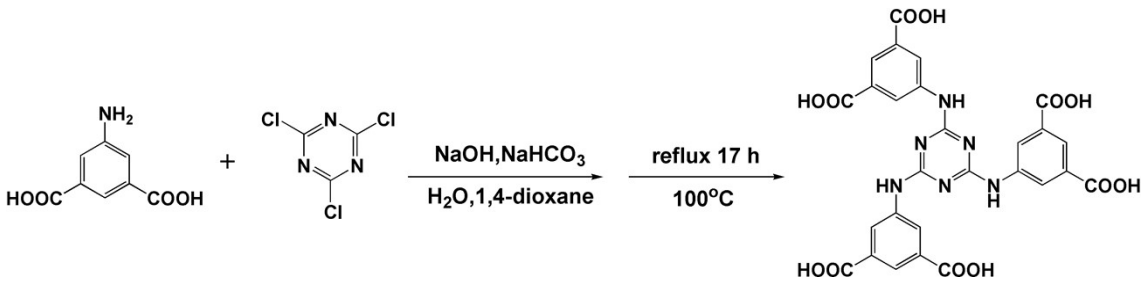

Scheme 1. The synthetic design of the ligand H_6TDPAT.

Electrochemical measurements.

Electrochemical CO_2RR performance measurements were performed using a CHI760E potentiostat or PINE AFCBP1 potentiostat with an H-cell or a flow cell. For experiments carried out in the H-cell, electrochemical testing was conducted using the CHI760E potentiostat. The gas-tight H-cell consists of two compartments separated by a Nafion membrane (N-117, DuPont). The electrolyte was 0.1 M $KHCO_3$. Pt mesh (1 cm×1 cm) and Ag/AgCl electrode (filled with saturated KCl

solution) were used as counter electrode and reference electrode, respectively. Before conducting the CO_2RR test, CO_2 was continuously bubbled into the electrolyte solution at a flow rate of 20 mL min^{-1} for at least 30 min to achieve CO_2 saturation. The pH of the 0.1 M $KHCO_3$ electrolyte saturated with CO_2 was about 6.82. Electrode potentials in this work were converted to reversible hydrogen electrode (RHE) using the following equation: $E_{(vs.\ RHE)} = E_{(vs.\ Ag/AgCl)} + 0.059 \times pH + 0.205$ V. During CO_2RR, the rate of CO_2 flow was maintained at 20 mL min^{-1}.

For the flow-cell experiment, electrolysis was conducted by using PINE AFCBP1 potentiostat. The flow cell consists of three compartments: gas chamber, catholyte chamber, and anolyte chamber. Catholyte and anolyte chambers were separated by an anion-exchange membrane (FAA-3-PK130, Fumapem). Ni foam (1 cm×1 cm) and Ag/AgCl electrode (filled with saturated KCl solution) were used as counter electrode and reference electrode, respectively. 1 M KOH solution was used as the catholyte and anolyte. The CO_2 flow rate was 10 mL min^{-1} during CO_2RR. The catholyte and anolyte are both circulated by the peristaltic pumps at 5 mL min^{-1}.

Products analysis.

The main products of CO_2RR on the CuxOy/CN catalyst were in the gas phase, so the analysis mainly focused on the gas phase products. The gas products were analyzed by GC7980 gas chromatograph (Shanghai Techcomp, China), equipped with the flame ionization detector (FID) for CO and hydrocarbons and a thermal conductivity detector (TCD) for H_2. Nitrogen was used as the carrier gas. The CO_2 gas was continuously purged at an average rate of 10 mL min^{-1} into the cathodic compartment and was routed into the gas chromatograph. The gas-phase products were analyzed at least 15 min after electrolysis to ensure that the CO_2RR reached a steady state.

The gas product Faradic efficiency was calculated by the following equation:[2]

$$FE_i = \frac{Q_i}{Q_{total}} = \frac{\frac{v \cdot x}{22400 \cdot 60} \cdot n \cdot F}{I} \quad (1)$$

Where FE_i represents the Faraday efficiency of a given gas product; i is the gas-phase product detected by GC; x is the concentration of gas-phase product measured by GC (in ppm); v is CO_2 feed rate; n_e is the electron transfer number of the gas-phase product generated during the

electrolysis of CO_2RR; F is the Faraday constant (96485 C mol^{-1}) of the gas-phase product; I is the total current of the CO_2RR electrolysis.

Materials Characterization.

Scanning electron microscopy (SEM) images were acquired on a NOVA NanoSEM 450 working at 3 kV. Transmission electron microscope (TEM), High-angle annular dark-field scanning transmission electron microscopy (HAADF-STEM), and the energy-dispersive X-ray spectroscope (EDS) images were obtained with JEM-F200 high-resolution transmission electron microscope working at 200 kV. The collection of powder X-ray diffraction (PXRD) data was performed on a Rigaku SmartLab 9 kW operating at 45 kV and 200 mA with a Cu Kα radiation source. The surface chemical states of the catalysts were analyzed by X-ray photoelectron spectroscopy (XPS), which was carried out on a Thermo ESCALAB250Xi spectrometer using monochromatic Al Ka radiation (1486.6 eV). GC7980 gas chromatograph (Shanghai Techcomp, China) was used to analyze the gas products.

***In-situ* ATR-SEIRAS measurements.**

In-situ attenuated total reflection surface-enhanced infrared absorption spectroscopy (ATR-SEIRAS) was measured by using a Nicolet 6700 (Thermo Fisher) equipped with a liquid nitrogen cooled MCT detector and a reflectance unit for the electrochemical cell at an incidence angle of 60°. 0.1M $KHCO_3$ electrolyte is used as the electrolyte in the spectral electrochemical cell, platinum sheet is used as the counter electrode, and Ag/AgCl is used as the reference electrode. The working electrode was prepared by dropping 30 μL of catalyst ink (5 mg mL^{-1}) onto the silicon crystal. The CO_2RR reaction lasts for 15 min at the potential of −1.1 V vs. RHE. Collect spectral signals after 1 min of reaction, with a data collection interval of 1 min. All spectra are given by absorbance -log (R/R_0) with a spectral resolution of 4 cm^{-1} for each curve.

***In-situ* Raman measurements.**

The *in-situ* Raman measurements were conducted using a Raman spectrometer (Renishaw, InVia) and a portable potentiostat (Ivium technology, Vertex). Custom-designed *in-situ* Raman cell, a 50× long working distance lens, and a 532 nm laser were employed to obtain operational surface-enhanced Raman spectroscopy (SERS). Ag/AgCl served as the reference electrode, and carbon cloth with a larger surface area served as the counter electrode. The working electrode was prepared on a glassy carbon substrate. The preparation method for the catalyst ink involved mixing 5 mg of

catalyst, 1 mL of EtOH, and 50 uL of Nafion solution, followed by 15 min of sonication. The prepared catalyst ink was drop-cast onto a 0.2 cm^2 glassy carbon with a loading of 1 mg cm^{-2}.

Density functional theory (DFT) calculations.

Density functional theory (DFT) calculations were performed by using the Vienna ab initio simulation package (VASP).[3-5] The electronic exchange and correlation were described by the Perdew-Burke-Ernzerhof (PBE) functional with the generalized gradient approximation.[6, 7] For the treatment of the interaction between the valence electrons and the ionic cores, the projector augmented-wave (PAW) method was used.[8] K-points were set at 2 × 2 × 1 on a Monkhorst-Pack grid, and a cut-off energy of 500 eV was adopted. Gaussian smearing scheme with a small SIGMA of 0.05 was applied. The spin polarisation effect has been taken into account. All DFT calculations were conducted with the aim of minimizing residual forces until the convergence criterion of 0.05 eV/Å was reached. The DFT-D3 approach proposed by Grimme et al[9] was adopted for vdW-dispersion energy correction.

Geometric structures of the catalysts were modeled using a (5 × 5) unit cell slab of Cu (1 0 0) (75 Cu atoms), with 18 H_2O and C_2N (40 C atoms and 20 N atoms), and at least15 Å vacuum space in the Z direction.

To compute the zero-point energy (ZPE), a finite differences approach was applied to displace mobile atoms in all directions by a small positive and negative displacement of 0.02 Å.

The Gibbs free energy differences (ΔG) including zero point energy (ZPE) and entropy corrections (TΔS) was calculated at 298.15 K:

$$\Delta G_i = \Delta E_i + \Delta ZPE_i - T\Delta S_i \quad (2)$$

Where ΔE_i is the energy difference of each reaction step.

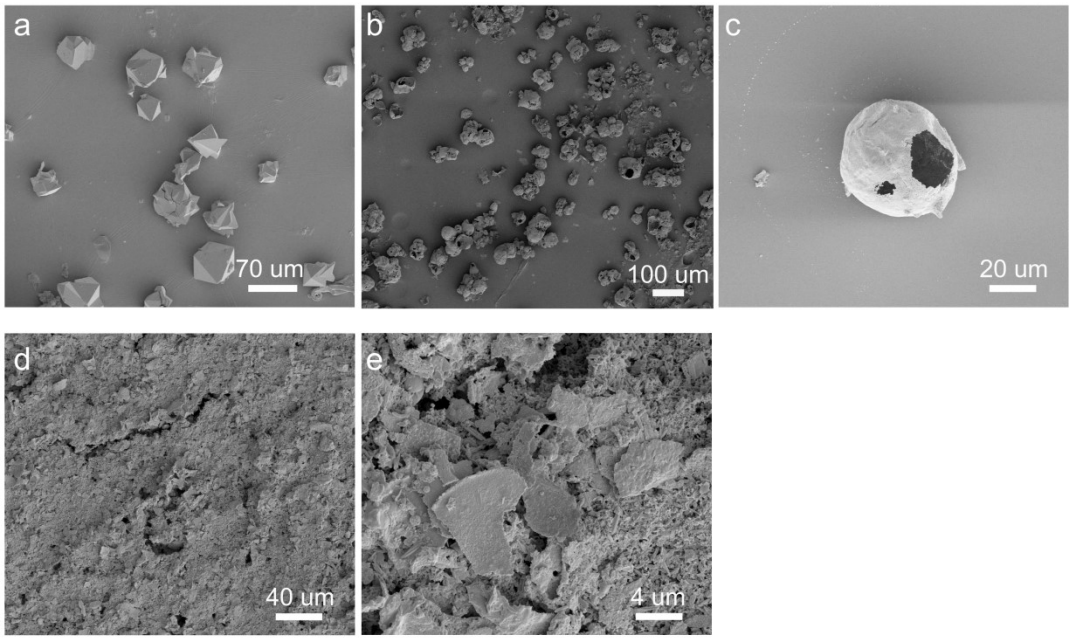

Figure S1. SEM images corresponding to different samples. (a) Cu MOF. (b-c) CuxOy/CN. (c-d) Working electrode prepared by CuxOy/CN catalyst.

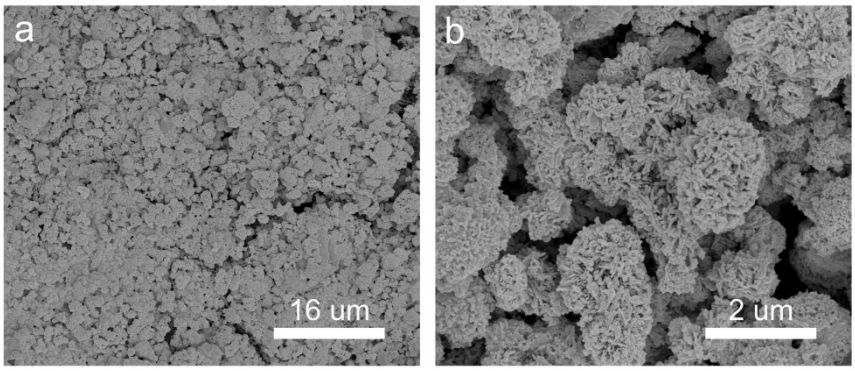

Figure S2. SEM images of commercial CuO control samples.

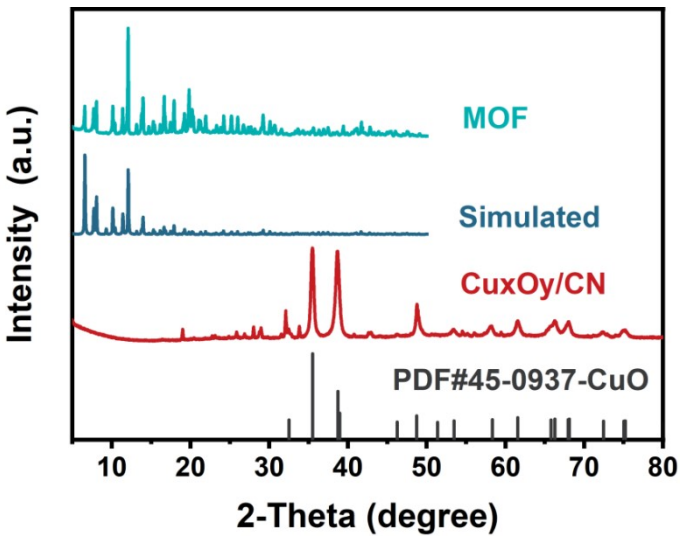

Figure S3. PXRD pattern of the simulated, as-synthesized MOF Cu-TDPAT, and CuxOy/CN.

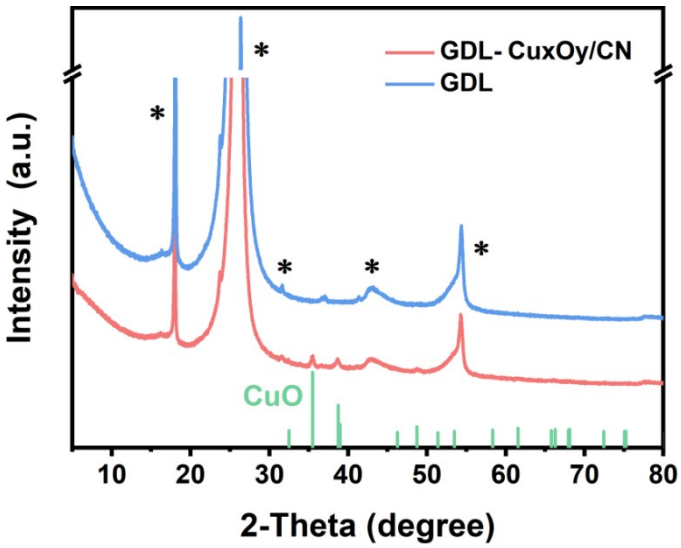

Figure S4. PXRD patterns of the gas diffusion layer (GDL) and the working electrode (denoted as GDL-CuxOy/CN) prepared by supporting the CuxOy/CN catalyst on the GDL substrate. Black symbols represent GDL features.

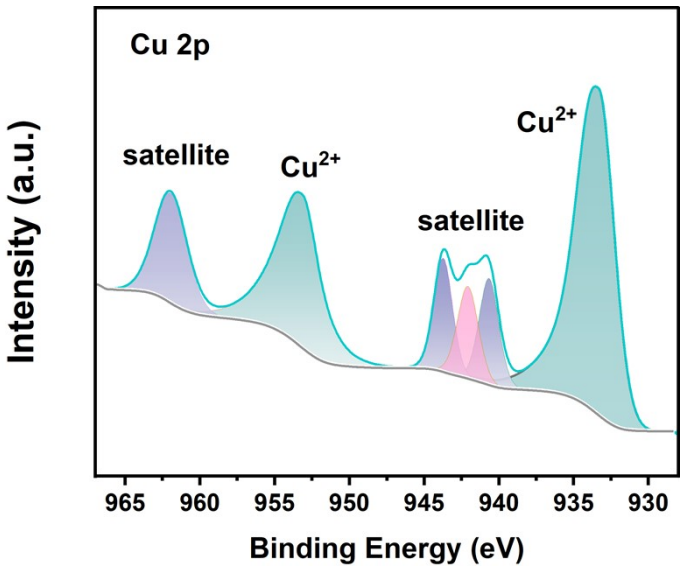

Figure S5. XPS spectra for the Cu 2p region of CuxOy/CN before CO_2RR.

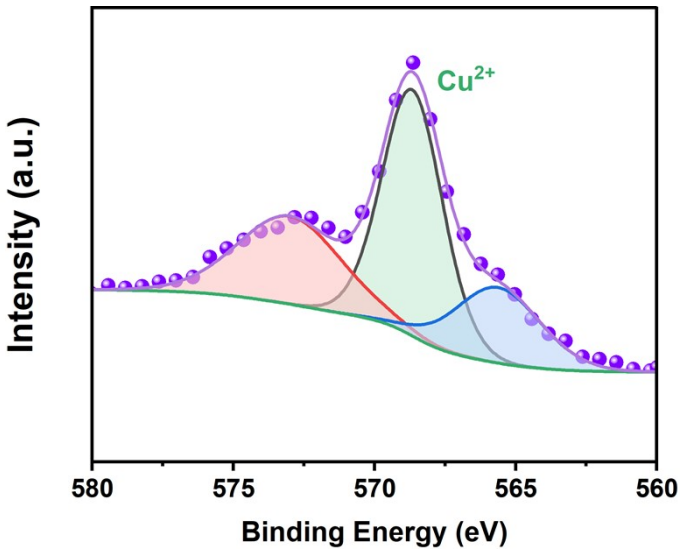

Figure S6. Cu LMM Auger spectra of CuxOy/CN before CO_2RR.

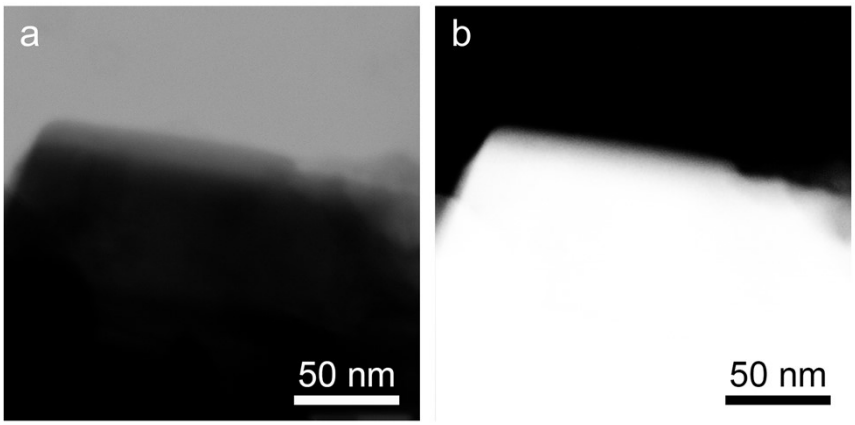

Figure S7. Bright-field scanning transmission electron microscopy (BF-STEM) and high-angle annular dark-field (HAADF) STEM images of the CuxOy/CN nanosheet shown in Figure 1b.

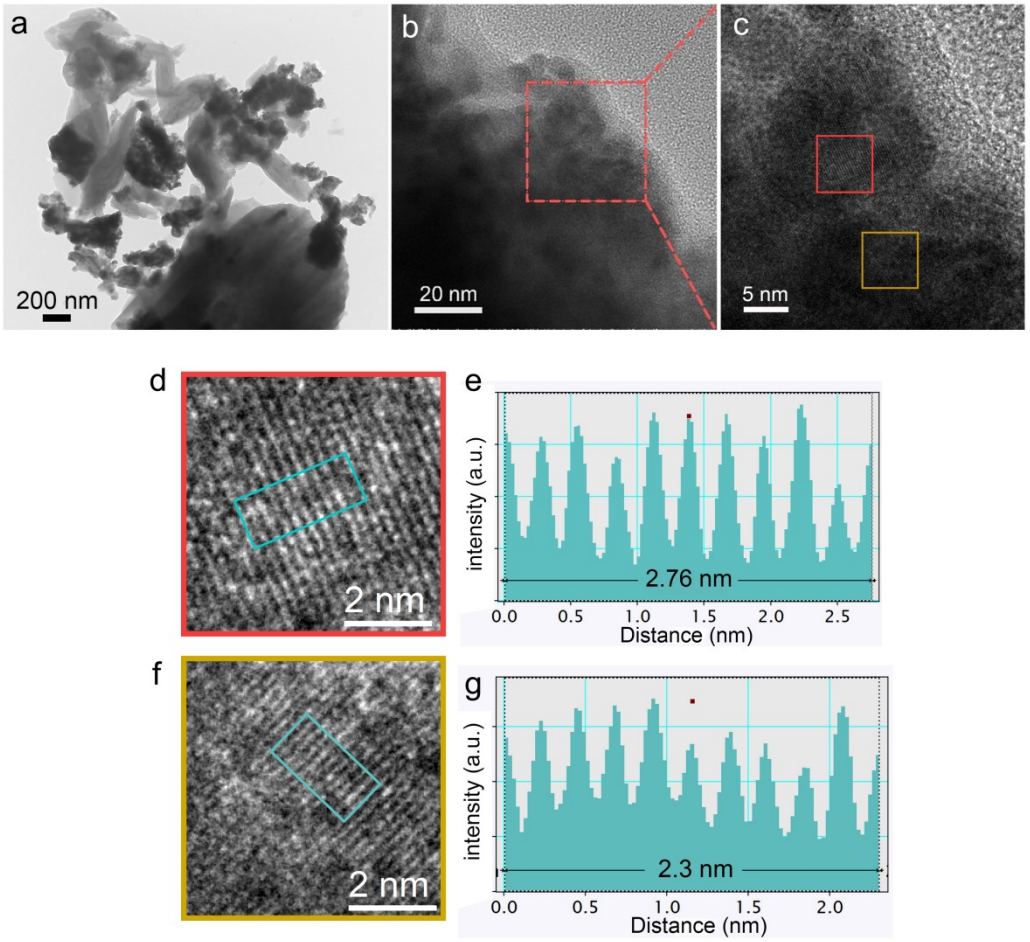

Figure S8. (a-c) HRTEM images of CuxOy/CN. (d) Enlarged image from the red box in (c). (f) Enlarged image from the yellow box in (c). (e) Intensity profiles measured from (d). (g) Intensity profiles measured from (f).

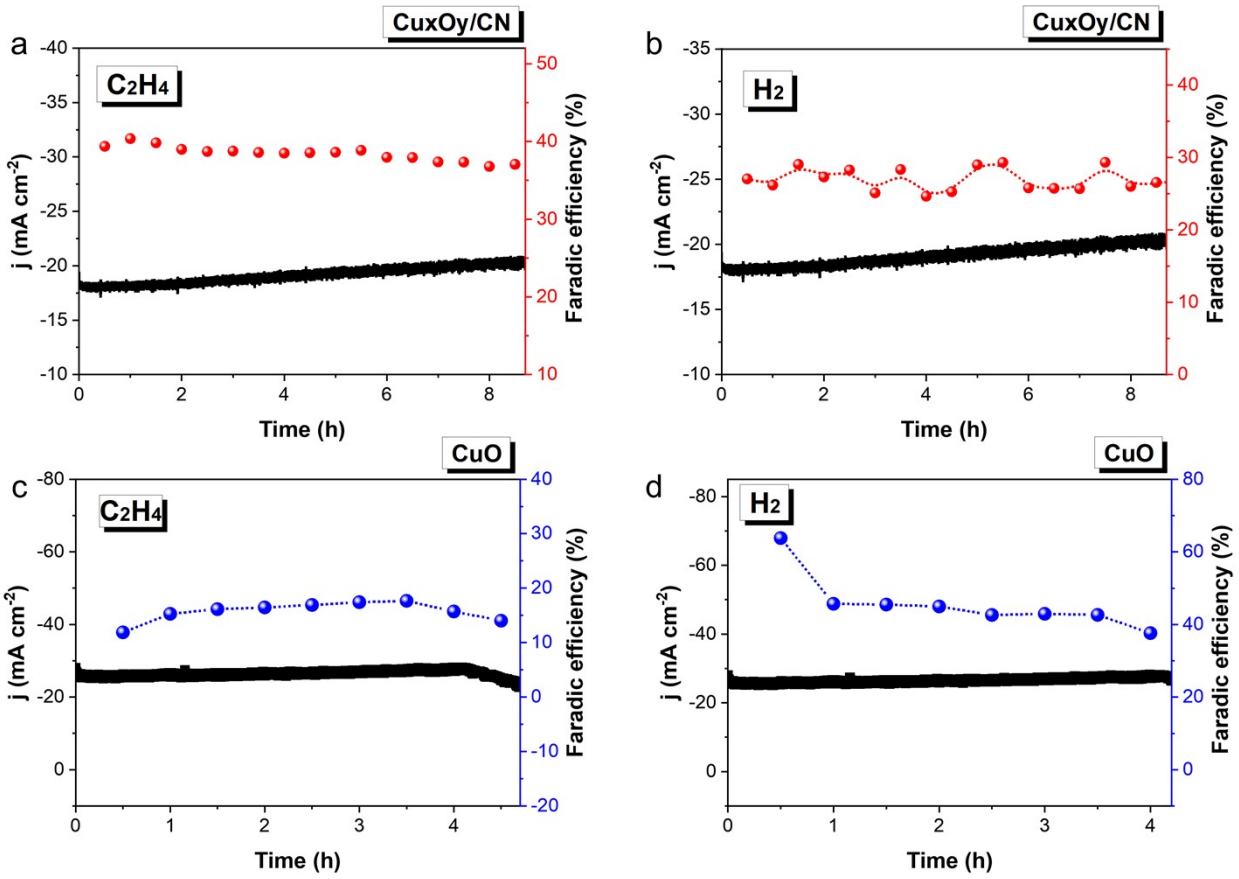

Figure S9. The total current density and FEs of C_2H_4 and H_2 catalyzed by commercial CuO and CuxOy/CN at different reaction times at the potential of −1 V vs. RHE in H-cell.

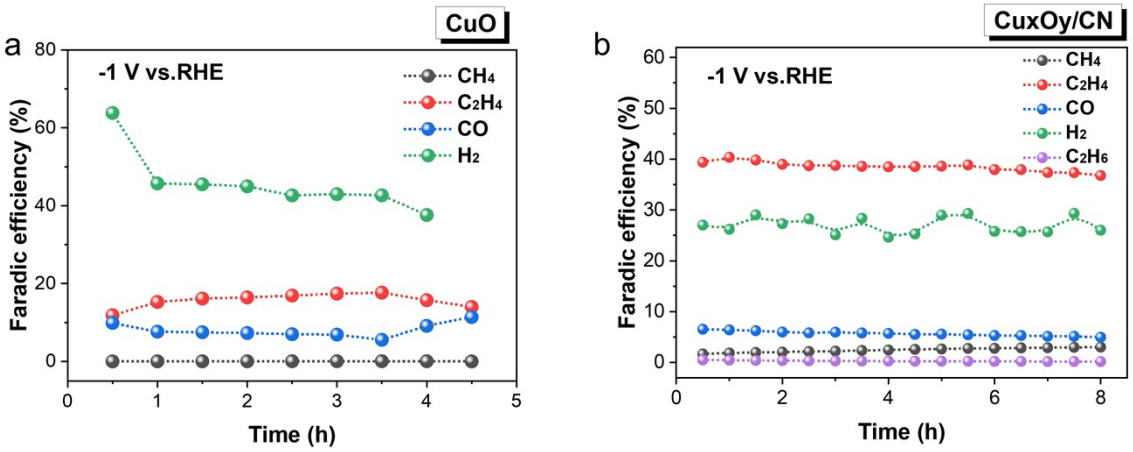

Figure S10. The FEs of main products catalyzed by commercial CuO and CuxOy/CN at different reaction times at the potential of −1 V vs. RHE in H-cell.

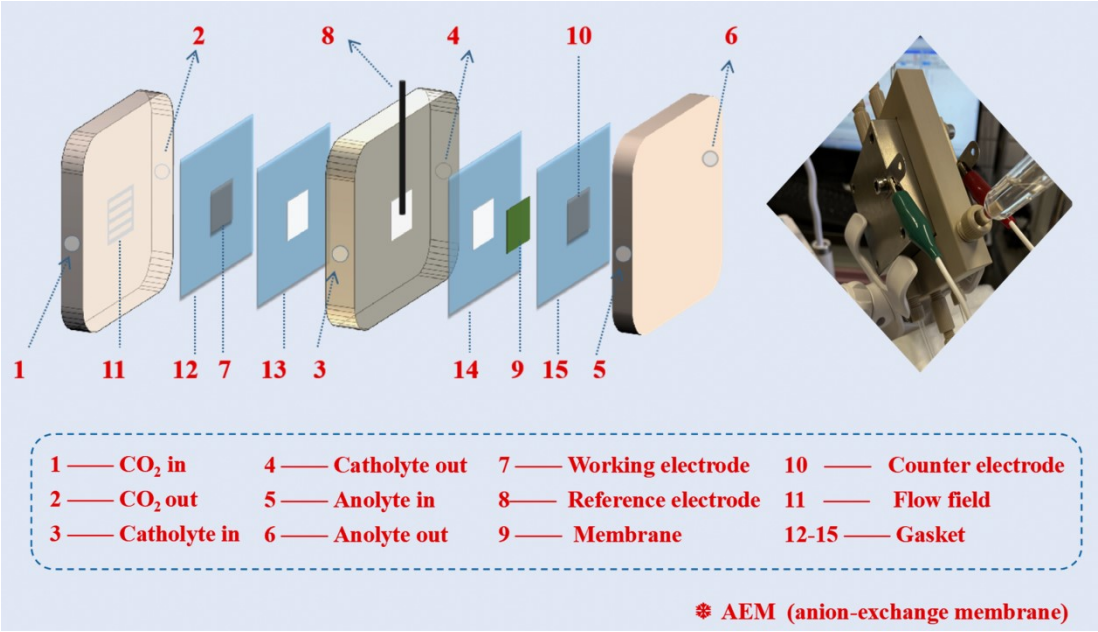

Figure S11. Scheme and photograph of the flow cell.

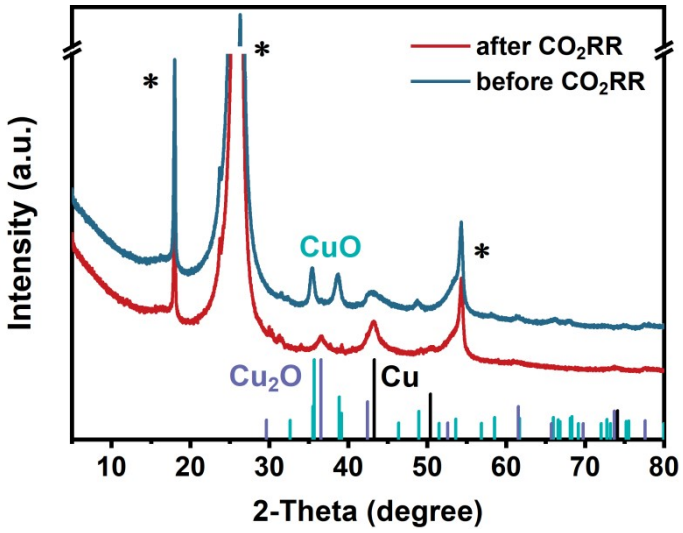

Figure S12. PXRD patterns of the commercial CuO before and after CO_2RR. Black symbols represent GDL features.

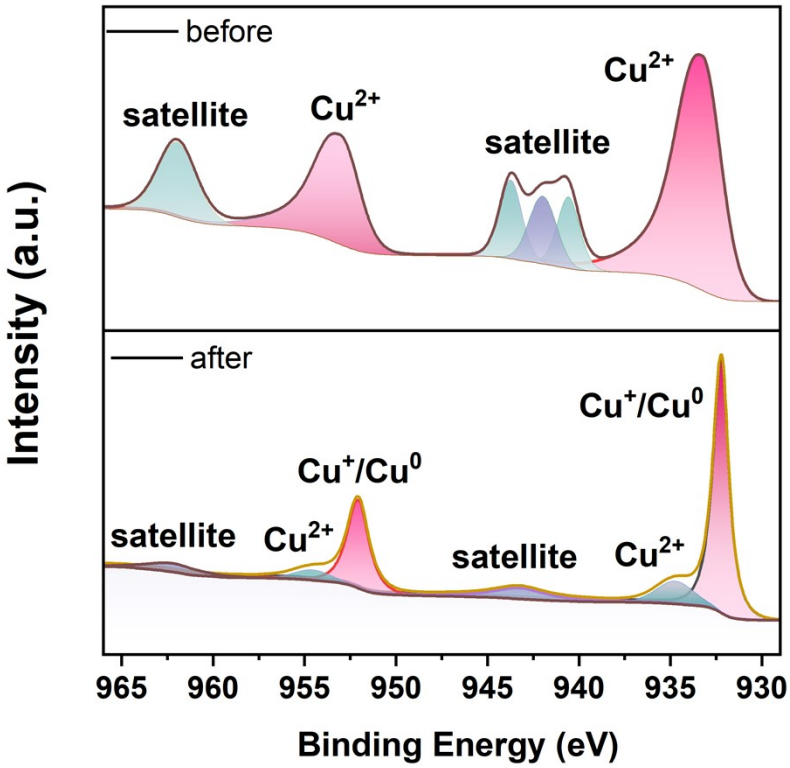

Figure S13. XPS spectra for the Cu 2p region of the commercial CuO before and after CO_2RR.

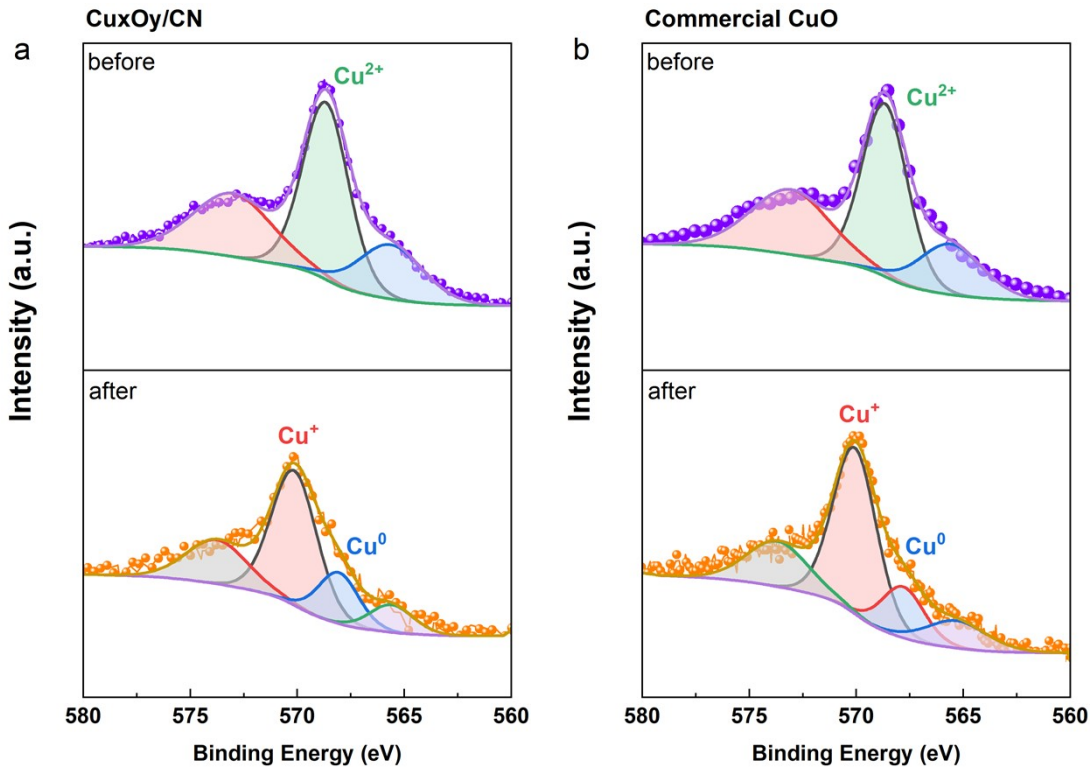

Figure S14. (a) Cu LMM Auger spectrum of CuxOy/CN before and after CO_2RR. (b) Cu LMM Auger spectrum of commercial CuO before and after CO_2RR.

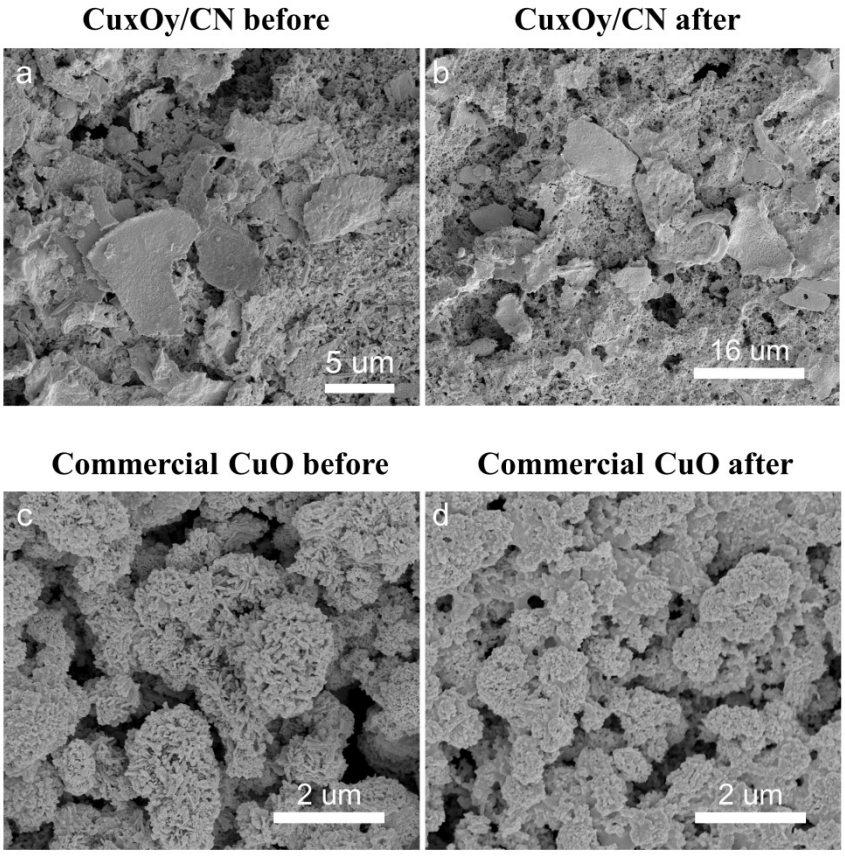

Figure S15. (a-b) SEM images of CuxOy/CN before and after CO_2RR. (c-d) SEM images of commercial CuO control samples before and after CO_2RR.

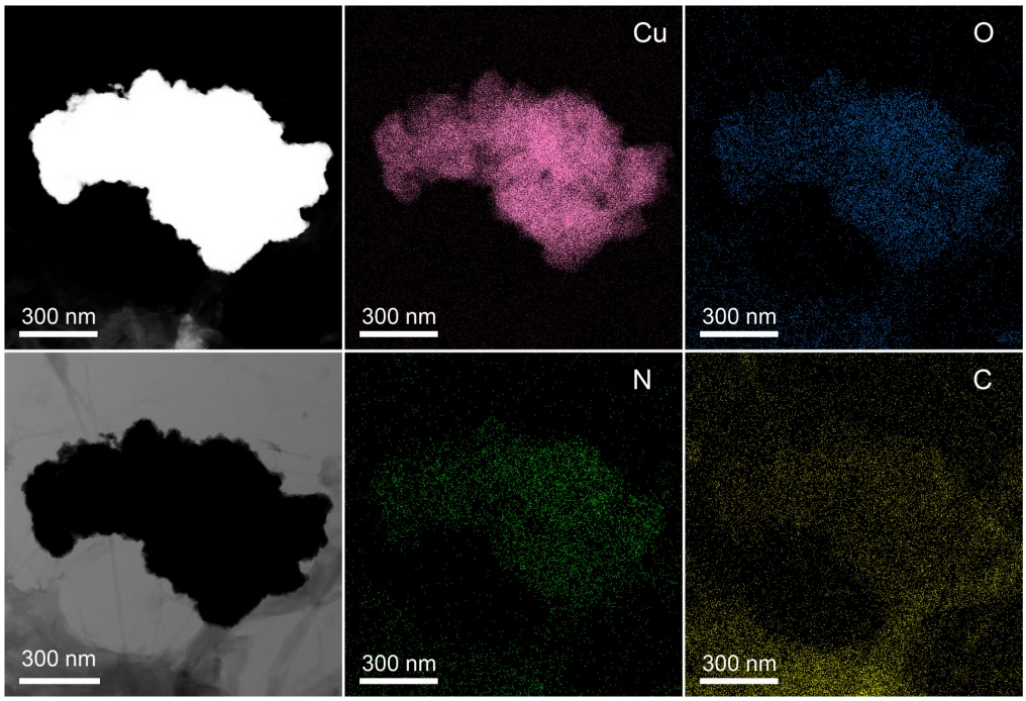

Figure S16. HAADF-STEM, BF-STEM, and EDS mapping images of the CuxOy/CN after CO_2RR.

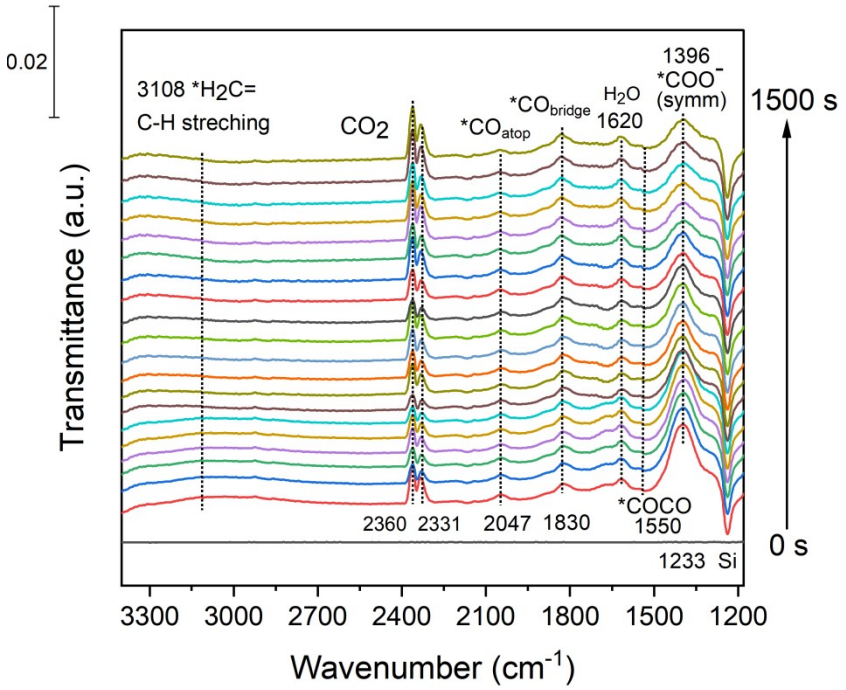

Figure S17. The *in-situ* ATR-SEIRAS spectra of CuxOy/CN.

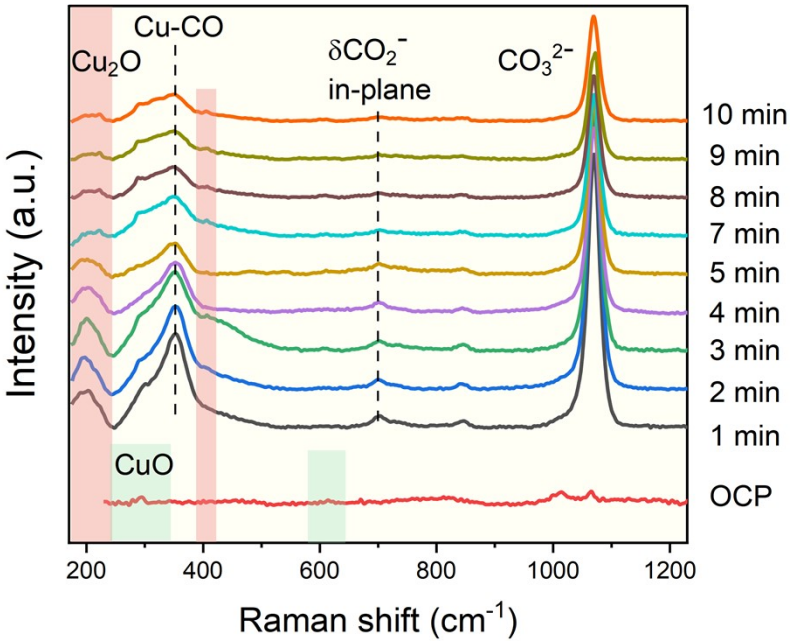

Figure S18. The *in-situ* Raman spectra of CuxOy/CN.

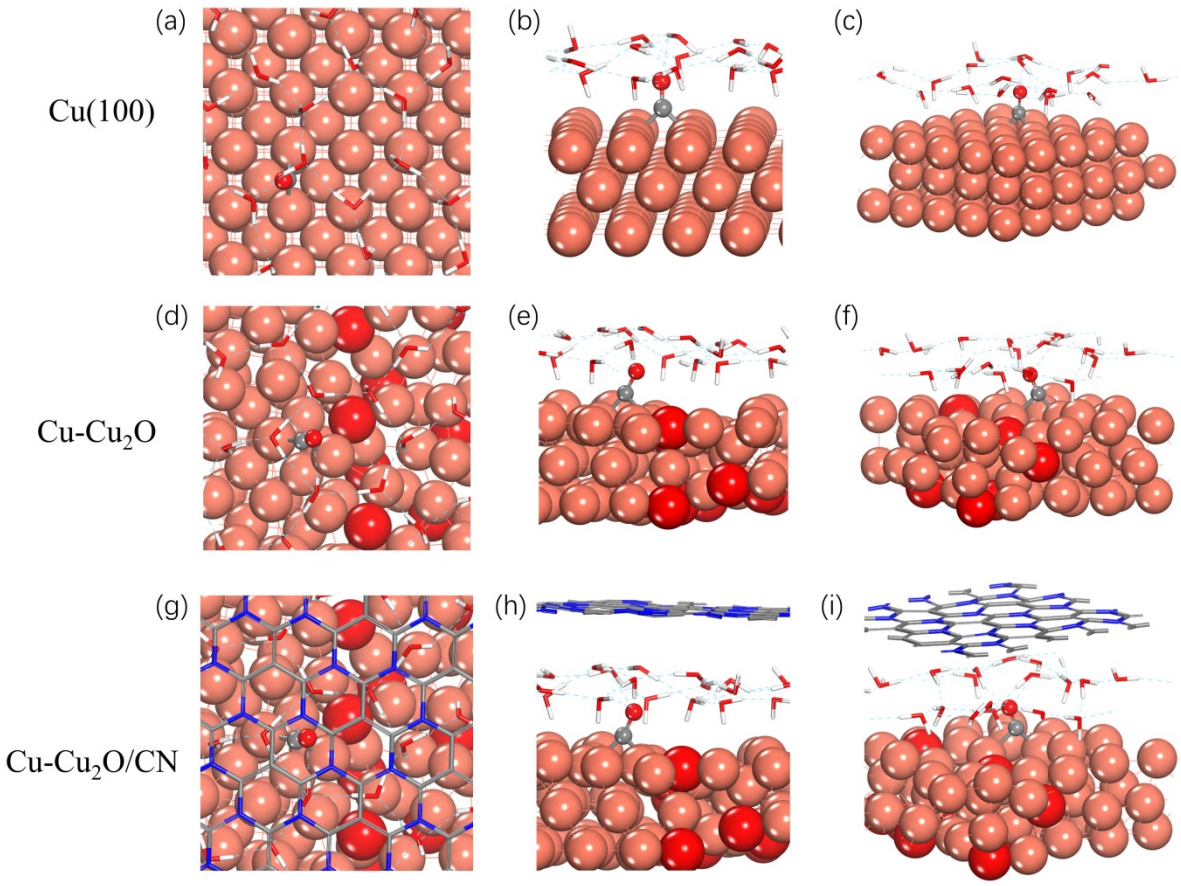

Figure S19. The geometries of key intermediate *CO_{bridge} on three structures: (a-c) Cu(100), (d-f) Cu-Cu_2O, and (g-i) Cu-Cu_2O/CN. Red, grey, white, and orange balls are oxygen, carbon, hydrogen, and copper, respectively. Water molecules are shown as red lines.

Table S1. Comparison of the performance of previously reported electrocatalysts for CO_2RR-to-ethylene.

Electrocatalyst	Faradaic efficiency [%]	Partial ethylene Current density [mA cm^{-2}]	Electrolyzer	Electrolyte	Reference
CuxOy/CN	41.7	10.2	H-cell	0.1 M $KHCO_3$	This work
	44	220	Flow cell	1 M KOH	This work
Cu_2O/NCS	24.7	10	H-cell	0.1 M $KHCO_3$	[10]
GB-Cu	38	40	Flow cell	1 M KOH	[11]
PROD-Cu-I	27.9	6.16	H-cell	0.1 M $KHCO_3$	[12]
Cu hollow multi-shell (HoMSs)	40	513.7	Flow-cell	0.5 M $KHCO_3$	[13]
$Cu(OH)_2$-D/Cu	41	18.4	H-cell	0.1 M $KHCO_3$	[14]
Cu_3N-Ag	36.6	26.7	Flow cell	1 M KOH	[15]
Cu_2O-BN	15	4.5	H-cell	0.5 M $KHCO_3$	[16]
Pd–Cu Janus	31.3	35	H-cell	0.5 M $KHCO_3$	[17]
OD-Cu-III	40	120	Flow-cell	1 M $KHCO_3$	[18]
Cu-MOF-CF	48.6	8.3	H-cell	0.1 M $KHCO_3$	[19]
C/Cu/HKUST-1/PTFE	54	138	MEA	0.1 M $KHCO_3$	[20]
Hierarchical Cu dendrites	31.8	79.5	Flow cell	1 M KOH	[21]
BIF-102NSs	11.3	N.A.	H-cell	0.5 M $KHCO_3$	[22]
CuBtz (HBtz = benzotriazole)	44	3.48	H-cell	0.1 M $KHCO_3$	[23]
CV-treated Cu	40	/	H-cell	0.1 M $KHCO_3$	[24]
Cu-PTFE NNs	45.4	300	Flow-cell	1 M KOH	[25]
MP-Cuf20	85.6	368	MEA	0.1 M $KHCO_3$	[26]
CuO-DDT	72	27.4	H-cell	0.1 M $KHCO_3$	[27]
	79.5	241.7	Flow cell	1 M KOH	
AN-Cu	38.1	7.3	H-cell	0.1 M $KHCO_3$	[28]
CuO−PVDF	40.6	11.7	H-cell	0.5 M $KHCO_3$	[29]
Cu-polyamine	87	N.A.	Flow cell	10 M KOH	[30]

References:

1. B. Li, Z. Zhang, Y. Li, K. Yao, Y. Zhu, Z. Deng, F. Yang, X. Zhou, G. Li, H. Wu, N. Nijem, Y. J. Chabal, Z. Lai, Y. Han, Z. Shi, S. Feng and J. Li, *Angew. Chem. Int. Ed.*, 2012, **51**, 1412-1415.
2. X. Zhang, H. Liu, J. Qin, H. Han, C. Qiu, S. Zhang, X. Hao, W. Liu and Y. Song, *Chem. Commun.*, 2019, **55**, 5659-5662.
3. G. Kresse and J. Hafner, *Physical Review B*, 1993, **48**, 13115-13118.
4. G. Kresse and J. Furthmüller, *Computational Materials Science*, 1996, **6**, 15-50.
5. G. Kresse and J. Hafner, *Physical Review B*, 1994, **49**, 14251-14269.
6. J. P. Perdew, K. Burke and M. Ernzerhof, *Phys. Rev. Lett.*, 1996, **77**, 3865-3868.
7. J. P. Perdew, K. Burke and M. Ernzerhof, *Phys. Rev. Lett.*, 1997, **78**, 1396-1396.
8. P. E. Blöchl, *Physical Review B*, 1994, **50**, 17953-17979.
9. S. Grimme, J. Antony, S. Ehrlich and H. Krieg, *The Journal of Chemical Physics*, 2010, **132**, 154104.
10. H. Ning, X. Wang, W. Wang, Q. Mao, Z. Yang, Q. Zhao, Y. Song and M. Wu, *Carbon*, 2019, **146**, 218-223.
11. Z. Chen, T. Wang, B. Liu, D. Cheng, C. Hu, G. Zhang, W. Zhu, H. Wang, Z.-J. Zhao and J. Gong, *J. Am. Chem. Soc.*, 2020, **142**, 6878-6883.
12. Z. Xie, Q. Wang, H. Yang, J. Feng, J. Chen, S. Song, C. Meng, K. Wang and Y. Tong, *Small*, 2024, **n/a**, 2401530.
13. C. Liu, M. Zhang, J. Li, W. Xue, T. Zheng, C. Xia and J. Zeng, *Angew. Chem. Int. Ed.*, 2022, **61**, e202113498.
14. D. Zhong, Z.-J. Zhao, Q. Zhao, D. Cheng, B. Liu, G. Zhang, W. Deng, H. Dong, L. Zhang, J. Li, J. Li

and J. Gong, *Angew. Chem. Int. Ed.*, 2021, **60**, 4879-4885.

15. J. Li, Y. Chen, B. Yao, W. Yang, X. Cui, H. Liu, S. Dai, S. Xi, Z. Sun, W. Chen, Y. Qin, J. Wang, Q. He, C. Ling, D. Wang and Z. Zhang, *J. Am. Chem. Soc.*, 2024, **146**, 5693-5701.
16. Y. Zhou, Y. Yao, R. Zhao, X. Wang, Z. Fu, D. Wang, H. Wang, L. Zhao, W. Ni, Z. Yang and Y.-M. Yan, *Angew. Chem. Int. Ed.*, 2022, **61**, e202205832.
17. Z. Lyu, S. Zhu, L. Xu, Z. Chen, Y. Zhang, M. Xie, T. Li, S. Zhou, J. Liu, M. Chi, M. Shao, M. Mavrikakis and Y. Xia, *J. Am. Chem. Soc.*, 2021, **143**, 149-162.
18. Z.-Z. Wu, X.-L. Zhang, Z.-Z. Niu, F.-Y. Gao, P.-P. Yang, L.-P. Chi, L. Shi, W.-S. Wei, R. Liu, Z. Chen, S. Hu, X. Zheng and M.-R. Gao, *J. Am. Chem. Soc.*, 2022, **144**, 259-269.
19. T. Yan, P. Wang and W.-Y. Sun, *Small*, 2023, **19**, 2206070.
20. D.-H. Nam, O. Shekhah, A. Ozden, C. McCallum, F. Li, X. Wang, Y. Lum, T. Lee, J. Li, J. Wicks, A. Johnston, D. Sinton, M. Eddaoudi and E. H. Sargent, *Adv. Mater.*, 2022, **34**, 2207088.
21. Z.-Z. Niu, F.-Y. Gao, X.-L. Zhang, P.-P. Yang, R. Liu, L.-P. Chi, Z.-Z. Wu, S. Qin, X. Yu and M.-R. Gao, *J. Am. Chem. Soc.*, 2021, **143**, 8011-8021.
22. P. Shao, W. Zhou, Q.-L. Hong, L. Yi, L. Zheng, W. Wang, H.-X. Zhang, H. Zhang and J. Zhang, *Angew. Chem. Int. Ed.*, 2021, **60**, 16687-16692.
23. H.-L. Zhu, H.-Y. Chen, Y.-X. Han, Z.-H. Zhao, P.-Q. Liao and X.-M. Chen, *J. Am. Chem. Soc.*, 2022, DOI: 10.1021/jacs.2c04670.
24. T.-C. Chou, C.-C. Chang, H.-L. Yu, W.-Y. Yu, C.-L. Dong, J.-J. Velasco-Vélez, C.-H. Chuang, L.-C. Chen, J.-F. Lee, J.-M. Chen and H.-L. Wu, *J. Am. Chem. Soc.*, 2020, **142**, 2857-2867.
25. B. Yang, K. Liu, H. Li, C. Liu, J. Fu, H. Li, J. E. Huang, P. Ou, T. Alkayyali, C. Cai, Y. Duan, H. Liu, P. An, N. Zhang, W. Li, X. Qiu, C. Jia, J. Hu, L. Chai, Z. Lin, Y. Gao, M. Miyauchi, E. Cortés, S. A. Maier

and M. Liu, *J. Am. Chem. Soc.*, 2022, **144**, 3039-3049.

26. J. Han, B. Tu, P. An, J. Zhang, Z. Yan, X. Zhang, C. Long, Y. Zhu, Y. Yuan, X. Qiu, Z. Yang, X. Huang, S. Yan and Z. Tang, *Adv. Mater.*, 2024, **n/a**, 2313926.
27. Y. Yao, T. Shi, W. Chen, J. Wu, Y. Fan, Y. Liu, L. Cao and Z. Chen, *Nat. Commun.*, 2024, **15**, 1257.
28. S. Y. Lee, H. Jung, N.-K. Kim, H.-S. Oh, B. K. Min and Y. J. Hwang, *J. Am. Chem. Soc.*, 2018, **140**, 8681-8689.
29. H.-Q. Liang, S. Zhao, X.-M. Hu, M. Ceccato, T. Skrydstrup and K. Daasbjerg, *ACS Catal.*, 2021, **11**, 958-966.
30. X. Chen, J. E. L. E. M. Chen, N. M. Alghoraibi, D. A. Henckel, R. Zhang, U. O. Nwabara, K. E. Madsen, P. J. A. Kenis, S. C. Zimmerman and A. A. Gewirth, *Nat. Catal.*, 2021, **4**, 20-27.